

AMSI
VACATION
RESEARCH
SCHOLARSHIPS

2017-2018



**Extracting coherently moving flow
structures from fluid flows**

Rose Crocker

Supervised by Associate Professor Sanjeeva Balasuriya
The University of Adelaide

Vacation Research Scholarships are funded jointly by the Department of Education and Training
and the Australian Mathematical Sciences Institute.



Australian Government
Department of Education and Training





Abstract

The equations governing the physics of fluids, with the exception of specific, simplified cases, are notoriously intractable. Their solutions, however, are of great importance in many fields of applied mathematics, including the modelling of geophysical flows, oceanic currents and atmospheric dynamics. It is often of interest to analyse a flow’s ‘coherent structures’, rather than seek specific solutions to its governing equations. Such analysis is of significance in many physical applications, such as in examining the extent to which an oil spill will spread, the transport of air pollution or heat flow in the atmosphere. In time-independent flows this is a fairly straight-forward process, however; add time-dependence and identifying flow barriers becomes a considerable challenge. This project investigates the theory and application of two mathematical techniques seeking to elucidate the coherent structures of time-dependent fluid flows, generally referred to as Lagrangian Coherent Structures (LCSs). The definition and requirements of an LCS are reviewed, and a brief overview of the suite of techniques available for extracting such structures. The Lagrangian-Averaged Vorticity Deviation (LAVD), a recent yet promising technique, and the Finite-Time Lyapunov Exponent (FTLE), a well-established technique, are employed to investigate the structure of classic vortical flows. The theory behind LAVD and FTLE is reviewed and applied to the numerical extraction of LCS in the double gyre and Rossby wave flow regimes.

1 Introduction

Mathematical analysis of the structure of fluid flows is essential in many physical applications. Such analysis is conceptually simple in steady flows, those governed by a time-independent differential equation of the form

$$\dot{\mathbf{x}} = \mathbf{v}(\mathbf{x}) \tag{1}$$

where $\dot{\mathbf{x}}$ is the time-derivative of the spatial co-ordinate vector \mathbf{x} . In such systems a common approach is to plot a *phase portrait*, a grid of spatial coordinates with vectors indicating the direction of the flow velocity vector field v at each point. Points $\hat{\mathbf{x}}$ for which $\mathbf{v}(\hat{\mathbf{x}}) = \mathbf{0}$ are called *fixed points* of the system; the nature of the fixed point present determines the flow structure surrounding the fixed point. Some examples of fixed point types include sources, sinks, saddle-points and centres, shown in Figure 1. Propitiously, in steady flows the phase space is identical to the physical space in which the fluid is flowing and level curves of the phase space represent fluid trajectories (Balasuriya, 2016). Hence, coherent flow structures may be identified directly from phase space analysis. Due to the nature of (1), these entities dictate distinct regions and boundaries in the flow that will exist for all time.

In unsteady systems, however; extraction of such flow structures becomes more complex. Such flows have time-dependent governing equations of the form

$$\dot{\mathbf{x}} = \mathbf{v}(\mathbf{x}, t) . \tag{2}$$

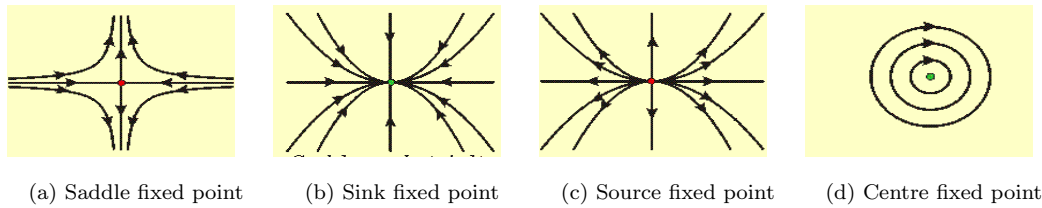


Figure 1: Four important types of fixed points and their local phase space trajectories. From <http://staff.www.ltu.se/~larserik/applmath/chap9en/part7.html>

Phase portraits of such flows may be constructed at a given time, giving an *Eulerian* picture of the system in which velocities are only dependent on the current position of fluid particles, without reference to their spatial evolution according to (2). With time-dependence, ‘fixed’ points are no longer fixed, and so the Eulerian approach of finding and classifying such points at a particular time may give misleading information about the flow structure (Balasuriya et al.). In the unsteady case we are more interested in *Lagrangian* methods; methods which incorporate fluid particle trajectories that are solutions to (2), thus accounting for the time-evolution of particle trajectories. In the steady case, where particle positions do not evolve with time, we expect structures arising from both approaches to be equivalent, while in the unsteady case the Lagrangian framework affords insight into the time evolution of the coherent structures we seek. Much research has focussed on Lagrangian methods for extracting structures from unsteady flows, formally known as *Lagrangian Coherent Structures* (LCS).

Before diving into the mathematical descriptions that have been derived for LCS, it is intriguing to consider their varied manifestations in the physical world. Jupiter’s Great Red Spot, for example, is an LCS comprising both a persistent vortex core and flow barrier demarcating the transition from rotational to laminar flow (Haller, 2015). This rotational structure, shown in Figure 2 a), is analogous to the centre fixed point structures of steady systems, yet is a structure resulting from time-dependent evolution. Another example emerges from a study of the Mexico Gulf Oil Spill, in which LCS theory was used to conceptualise the structural changes observed as the oil cloud spread (Mezic et al., 2010). Figure 2 c) shows a sudden extension of the oil cloud which is analogous to the saddle-point structures of steady systems yet is clearly time-dependent. LCS theory is also routinely used to model atmospheric dynamics, ocean gyres and geophysical flow patterns (Balasuriya, 2016). LCS analysis techniques have even been applied to the investigation of how marine predators track the living dynamic structures created by schools of fish in the ocean (Kew et al., 2009). Considering these applications of LCS theory, two key points emerge. Firstly, the diversity of the physical structures considered demand a theory suitably general to encompass all those we aim to describe in nature. Secondly, we can often draw analogies to steady flow structures in seeking unsteady structures. In the unsteady case; however, the time Lagrangian evolution of structures must now be taken into account. This requires us to consider the *flow map* associated with (2).

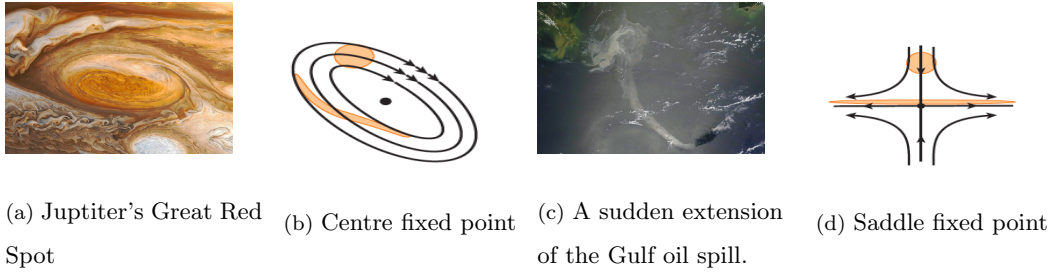


Figure 2: Examples of some coherent flow structures in unsteady flows for which we can draw analogies with common steady flow structures (Haller, 2015).

2 Defining LCS

2.1 Relation to the flow map

Unlike in defining the sink, source and saddle-point structures of steady systems, there is no absolute definition for an LCS. Balasuriya et. al. (), however, attempt to set out a very general framework for defining LCS which will be discussed. As the name suggests, LCS are generally conceptualised as “coherent” objects emergent in the visualisation of the Lagrangian trajectories of (2). Intuitively, these objects should be generalisations of recognised, persistent flow structures, such as eddies, vortices and jets. The particular properties used to make such a generalisation determine the definition of LCS applied in the context at hand. Due to the finite-time limitations of real-world datasets, and the disparity of finite versus infinite time flow behaviour, LCS are defined within a finite time slice $[-T, T]$, which is itself a subset of Ω , the flow domain over all time. We may attempt to extract the LCS for a time interval $[t_0, t] \in [-T, T]$ by first considering the Lagrangian form of the flow map. The flow map is in Lagrangian form when it is dependent on the initial positions of fluid particles. In this form, the flow map is defined as

$$\mathcal{F}_{t_0}^t(\mathbf{x}_0) := \mathbf{x}(t_0; t, \mathbf{x}_0), \quad (3)$$

with respect to solutions $\mathbf{x}(t_0; t, \mathbf{x}_0)$ to (2) obeying the initial condition $\mathbf{x}(t_0; t_0, \mathbf{x}_0) = \mathbf{x}_0$ and for which the flow domain at time t may be denoted $U(t) \in \Omega$ (Haller, 2015).

The flow map takes the set of initial particle positions $\mathbf{x}_0 \in U(t_0)$ and evolves these positions to time t according to the flow's governing differential equation, (2). This evolution may be in forward or backward time, as (2) is time-reversible and, accordingly, the flow map is invertible. Following Balasuriya et. al.'s set up (), we also require that the fluid velocity field \mathbf{v} have continuous spatial and temporal derivatives and that all fluid particle trajectories are defined and unique for all initial conditions in Ω .

Accepting these requisites, an LCS can be thought of as a subset of Ω , extracted at a time $t \in [-T, T]$. Accordingly, an LCS is thus dependent on not just the final time considered but the time interval. The LCS itself



may be identified according to some criterion imposed on the behaviour of the flow map $F_{t_0}^t(\mathbf{x}_0)$. For example, an LCS could be the subset $S \in \Omega$ such that $F_{t_0}^t(S)$ is sufficiently similar to S as defined by connectivity and minimal filamentation of the boundary ∂S in the time interval. Such criterion would select for structures like vortex cores, which often possess a coherent central structure surrounded by a filamenting boundary surface. Another example is seeking S such that $F_{t_0}^t(S)$ is much more strongly attracting than other sets of particles in the neighbourhood of S . These criterion would seek to divide the fluid domain into coherent regions with barriers of maximal stretching dividing the regions.

It follows that, in a very abstract sense, LCS may be defined as structures resulting from the application of criteria via some procedure \mathcal{P} , i.e.,

$$LCS(t_0, t) := \mathcal{P}(F_{t_0}^t(\mathbf{x}))$$

where $LCS(t_0, t)$ is a subset of Ω . The selection of specific criterion and computational procedures capable of applying such criterion to the flow map has led to the development of many LCS extraction techniques. Simply satisfying this generalised definition however, a technique may not necessarily provide useful information on the structure of a flow. Researchers such as Haller (2015) have investigated what mathematical requirements are necessary for a technique to be broadly applicable to important flow regimes.

2.2 LCS requirements

Aiming to standardise LCS extraction techniques, Haller sets out a series of requirements which an LCS theory must satisfy (2015). These requirements attempt to set a benchmark in the construction of techniques seeking to extract LCS from both analytic and data-based flows.

1. *Objectivity*: Objectivity requires that the LCS theory from which an extraction technique is derived be independent of the frame of reference. Mathematically, this is the requirement that an LCS theory's conclusions be invariant under Euclidean coordinate changes of the form

$$\mathbf{y} = Q(t)\mathbf{x} + \mathbf{p}(t)$$

where $Q(t)$ is a time-dependent rotational tensor and $\mathbf{p}(t)$ is a time-dependent translation. It has been found that, without this requirement, false positives in LCS extraction may occur, such as when the reference frame is itself rotating with the flow.

2. *Finite Time*: Many flows evolve aperiodically in a finite time-span and so the infinite time behaviour of such flows is not indicative of the finite time behaviour. Ideally, we seek to extract structures that evolve coherently on finite time scales.
3. *Lagrangian Invariance*: An LCS theory must track the evolution of a material surface with the flow. I.e. structures obtained at different initial times t_0 must pertain to the same finite-time dynamical system and evolve into each other.



4. *Spatial Convergence*: For a smooth velocity data set the flow map is a smooth function of initial conditions over finite times.

2.3 Overview of the LCS extraction methods used

Many methods have been derived to extract LCS according to particular structural criteria, not all of which satisfy Haller’s requirements for an LCS (2015). Following the generalised definition of an LCS as a structure extracted via a procedure which applies a criterion to the flow map, computational extraction methods generally select an initial grid of particle positions, evolve these positions forward in time via the flow map and then seek a subset of the map satisfying a criterion. There are, for example, trajectory average techniques (Balasuriya et al.), which compute the average of some observable property of the flow map, such as the velocity field, over the interval (t_0, t) . Such a technique then uses a criterion which seeks structures with local observable properties significantly differing from the average. Another example is a variational approach, which seeks the most repelling or attracting material surfaces advected by the flow field, as identified from variational calculus methods. There are also a variety of techniques which seek LCS based on measures of mixing, such as the finite-time entropy. Certain techniques may be more effective than others on particular flow regimes or for analytic or data-based flows.

In this project two techniques for LCS extraction are considered. One of these, the Finite Time Lyapunov Exponent (FTLE), is perhaps the most established of computational LCS extraction methods, as it is effective in a variety of important flow regimes and is fairly simple to implement (Shadden et al., 2005). The other, the Lagrangian Averaged Vorticity Deviation (LAVD), is relatively recent and much less common in the literature (Haller et al., 2016). These techniques both seek to extract coherent flow structures, yet focus on different aspects of fluid flow properties; that is, different criterion and procedures for LCS extraction. The FTLE identifies regions of significant exponential stretching of fluid particles, so that a high FTLE field often indicates barriers between distinct regions of the flow. This technique is effective for flows where particles are stretched as the fluid is advected, but will not identify structures arising from purely rotational dynamics. Conversely, LAVD focusses on the vortical properties of fluid flow, seeking to extract such rotational structures as vortices and eddies. The comparison of these techniques may afford insight into both boundaries and rotational structures in fluid flow.

3 The Finite-Time Lyapunov Exponent (FTLE)

An oft cited formulation of LCS is that proposed by Haller (2015). In this approach we consider a time-dependent material surface $\mathcal{M}(t)$ and the flow map (3). From the flow map definition, a material surface $\mathcal{M}(t_0)$ evolved to time t will be

$$\mathcal{M}(t) = \mathcal{F}_{t_0}^t(\mathcal{M}(t_0))$$



In extracting LCS we seek to extract material structures with an *exceptional* impact on the deformation of nearby fluid elements. Generally, fluid element demormation is quantified using the Cauchy-Green strain tensor, $\mathcal{C}(\mathbf{x}_0)$, defined as

$$\mathcal{C}(\mathbf{x}_0) = [\nabla \mathcal{F}_{t_0}^t(\mathbf{x}_0)]^T \nabla \mathcal{F}_{t_0}^t(x_0)$$

which is a symmetric, positive definite tensor describing the strain undergone by a fluid element dependent on its initial position. A fluid element can be thought of as a vanishingly small fluid particle which may be deformed as the flow velocity field acts upon it.

FTLE approaches use this definition in the extraction of LCS. We consider a time-dependent perturbation about the spatial coordinate vector \mathbf{x} , $\delta\mathbf{x}(t)$, so that at time t , $\mathbf{y} = \mathbf{x} + \delta\mathbf{x}(t)$ is the new position. Hence, using the Taylor series expansion for the flow map about \mathbf{x} we have that the deviation between trajectories at time t is

$$\delta\mathbf{x}(t) = \mathcal{F}_{t_0}^t(\mathbf{y}) - \mathcal{F}_{t_0}^t(\mathbf{x}) = \nabla \mathcal{F}_{t_0}^t(\mathbf{x})\delta\mathbf{x}(0) + \mathcal{O}(\|\delta\mathbf{x}(0)\|^2)$$

From this formulation, the magnitude of the perturbation is given by the standard Euclidean norm:

$$\|\delta\mathbf{x}(t)\| = \sqrt{\left\langle \delta\mathbf{x}(0), \frac{d\mathcal{F}_{t_0}^t(\mathbf{x})^*}{d\mathbf{x}} \frac{d\mathcal{F}_{t_0}^t(\mathbf{x})}{d\mathbf{x}} \delta\mathbf{x}(0) \right\rangle}$$

where $*$ denotes the adjoint.

$\frac{d\mathcal{F}_{t_0}^t(\mathbf{x})^*}{d\mathbf{x}} \frac{d\mathcal{F}_{t_0}^t(\mathbf{x})}{d\mathbf{x}}$ corresponds to the Cauchy-Green strain tensor evaluated at \mathbf{x} , $\mathcal{C}(\mathbf{x})$. As $\|\delta\mathbf{x}(t)\|$ is a matrix norm, by definition it can be written as

$$\|\delta\mathbf{x}(t)\| = \sqrt{\lambda_{max}(\mathcal{C}(\mathbf{x}))}$$

$\sqrt{\lambda_{max}}$ can be thought of as an operator on $\|\delta\mathbf{x}(t)\|$ which yields its maximum at time t , such that

$$\max_{\delta\mathbf{x}(0)} \|\delta\mathbf{x}(t)\| = \sqrt{\lambda_{max}(\mathcal{C}(\mathbf{x}))} \|\bar{\delta\mathbf{x}}(0)\|$$

where $\|\bar{\delta\mathbf{x}}(0)\| \neq 0$ and $\bar{\delta\mathbf{x}}(0)$ is aligned with the eigenvector corresponding to $\lambda_{max}(\mathcal{C}(\mathbf{x}))$ (Horn and Johnson, 1985). This can be rewritten as

$$\max_{\delta\mathbf{x}(0)} \|\delta\mathbf{x}(t)\| = e^{FTLE(\mathbf{x}, t_0, t)} \|\bar{\delta\mathbf{x}}(0)\|$$

where

$$FTLE(\mathbf{x}, t_0, t) = \frac{1}{|t - t_0|} \ln(\sqrt{\lambda_{max}(\mathbf{x}, t_0, t)}) \quad (4)$$

which is the FTLE field calculated for the time interval $[t_0, t]$. $\lambda_{max}(\mathbf{x})$ corresponds to the maximal stretching at a point \mathbf{x} . The FTLE value for \mathbf{x} gives the exponent of exponential stretching over the time interval $[t_0, t]$. FTLE ‘ridges’, that is, regions of conspicuously high FLTE values are regions of maximal stretching of nearby fluid elements. Although not suitable in all flow regimes, FTLE provides useful insight into extant LCS in many important flows.



4 The Lagrangian-Averaged Vorticity Deviation (LAVD)

To derive the LAVD formula we consider the decomposition of the flow map into the pure strain tensor $\mathbf{M}_{t_0}^t$ and the pure rotational tensor $\mathbf{O}_{t_0}^t$.

$$\mathcal{F}_{t_0}^t = \mathbf{O}_{t_0}^t \mathbf{M}_{t_0}^t$$

The rotational tensor describes fluid element rotation but is not objective. The rotational tensor may also be factorised into two deformation gradients: a spatially uniform rotation gradient $\Theta_{t_0}^t$, which is the proper orthogonal mean-rotation tensor, and a gradient describing deviations from uniform flow, $\Phi_{t_0}^t$, the proper orthogonal relative rotation tensor. I.e., $\mathbf{O}_{t_0}^t$ may be written,

$$\mathbf{O}_{t_0}^t = \Phi_{t_0}^t \Theta_{t_0}^t$$

The relative rotation tensor is dynamically consistent, meaning that the following holds:

$$\Phi_{t_0}^t = \Phi_{t_0}^s \Phi_s^t,$$

for some $s \in [t_0, t]$. This dynamic consistency implies that the total angle traced out by the tensor around its axis of rotation, $\psi_{t_0}^t(\mathbf{x}_0)$ is also dynamically consistent, implying that

$$\psi_{t_0}^t(\mathbf{x}_0) = \psi_{t_0}^s(\mathbf{x}_0) + \psi_s^t(\mathbf{x}_0)$$

It has been shown that $\psi_{t_0}^t(\mathbf{x}_0)$ is objective in two and three dimensions, as per Haller's requirements for an LCS theory

Haller et al. (2016).

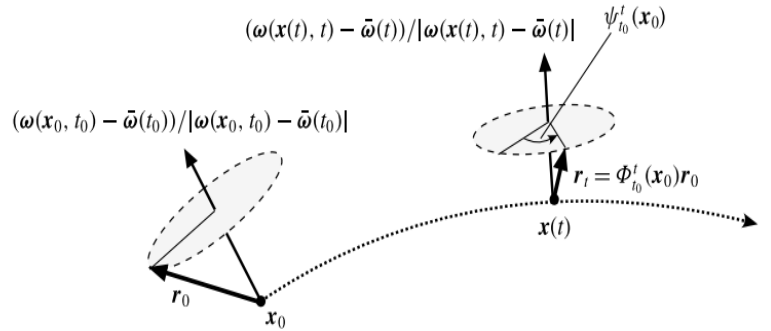


Figure 3: Geometry of the intrinsic rotation angle $\psi_{t_0}^t(\mathbf{x}_0)$ along a material trajectory $\mathbf{x}(t)$ (Haller et al., 2016)

Considering the geometry of the proper orthogonal relative rotation tensor (See Figure 3), $\psi_{t_0}^t(\mathbf{x}_0)$ may be computed as

$$\psi_{t_0}^t(\mathbf{x}_0) = \frac{1}{2} LAVD_{t_0}^t(\mathbf{x}_0)$$

with

$$LAVD_{t_0}^t(\mathbf{x}_0) := \int_{t_0}^t |\omega(\mathbf{x}(s; \mathbf{x}_0) - \bar{\omega}(s))| ds$$

and

$$\bar{\omega}(s) = \frac{\int_{U(t)} \omega(\mathbf{x}, t) dV}{vol(U(t))}$$

where $vol()$ denotes area for two-dimensional flows and volume for three-dimensional flows and dV similarly denotes the volume element for three-dimensional flows and the area element for two-dimensional flows. The



symbol ω is the vorticity, $\omega = \nabla \times \mathbf{v}$ (Haller et al., 2016).

As this formulation focusses on the rotational component of the flow map, the LAVD technique seeks to extract LCS as regions of the flow map for which there is coherent rotational behaviour. As such, the structures extracted via LAVD satisfy a very different definition of coherence to those extracted via FTLE techniques, providing complementary information on the flow structure.

5 Numerical Implementation

5.1 Algorithms to implement FTLE

The FTLE is a well established technique and its numerical implementation is reasonably straight forward. MATLAB code was written which estimates $\nabla \mathcal{F}_{t_0}^t = [\mathcal{F}_1 \mathcal{F}_2]$ using a first order finite difference scheme over a grid of initial coordinates. It then calculates the Cauchy-Green strain tensor at each spatial point as

$$\mathcal{C}(\mathbf{x}_0) = \begin{bmatrix} \left(\frac{\partial \mathcal{F}_1(\mathbf{x}_0)}{\partial x_1}\right)^2 + \left(\frac{\partial \mathcal{F}_1(\mathbf{x}_0)}{\partial x_2}\right)^2 & \frac{\partial \mathcal{F}_1(\mathbf{x}_0)}{\partial x_1} \frac{\partial \mathcal{F}_1(\mathbf{x}_0)}{\partial x_2} + \frac{\partial \mathcal{F}_2(\mathbf{x}_0)}{\partial x_1} \frac{\partial \mathcal{F}_2(\mathbf{x}_0)}{\partial x_2} \\ \frac{\partial \mathcal{F}_1(\mathbf{x}_0)}{\partial x_1} \frac{\partial \mathcal{F}_1(\mathbf{x}_0)}{\partial x_2} + \frac{\partial \mathcal{F}_2(\mathbf{x}_0)}{\partial x_1} \frac{\partial \mathcal{F}_2(\mathbf{x}_0)}{\partial x_2} & \left(\frac{\partial \mathcal{F}_2(\mathbf{x}_0)}{\partial x_1}\right)^2 + \left(\frac{\partial \mathcal{F}_2(\mathbf{x}_0)}{\partial x_2}\right)^2 \end{bmatrix}$$

MATLAB's `eigs()` function is then called to find the maximum eigenvalue for $\mathcal{C}(\mathbf{x}_0)$ and hence the value of (4) at each spatial coordinate. Although straight forward to implement, this algorithm is computationally time consuming due to the necessity of evaluating a matrix at each spatial coordinate. Possibly other methods could be used to estimate $\mathcal{C}(\mathbf{x}_0)$ and cut down computational time, but this method was sufficient for the needs of this project.

5.2 Algorithms to implement LAVD

In comparison to the FTLE field, the LAVD field formulation is not so straight forward to implement numerically and so a major focus of the project was developing methods to numerically implement LAVD. There are three main parts to the numerical implementation which require discernment in the selection of appropriate numerical methods. Firstly, the set of initial spatial coordinates $U(t_0)$ must be advected according to the velocity field to compute $\mathbf{x}(t_0; t, \mathbf{x}_0) \in U(t)$. Rather than implement an inbuilt MATLAB ODE solver, a function which uses the fourth order explicit Runge-Kutta method to time evolve the particle positions was written. This allowed avoidance of the dynamically varied timesteps implicit in many MATLAB solvers which, although useful for stiff ODEs, would significantly complicate the following numerical integration.

Secondly, the spatial average of the vorticity, $\bar{\omega}$ must be calculated. Calculating this quantity for time-dependent domains, such as Rossby wave flow, is rather non-trivial and various approaches were considered. Initially code was written to interpolate the value of ω evaluated at the final particle positions back onto the initial grid, which is evenly spaced and hence conducive to straightforward numerical integration methods. However, over larger timespans flows with time-dependent domains generally stray so far from the initial grid that



interpolation becomes restrictively inaccurate. A method trialled to overcome this is to seek a rectangular domain encapsulating the particles at a time t after t_0 and interpolate ω at t onto this new rectangular grid. However, the evolved flow domain often becomes considerably non-convex and translation of the interpolation grid may still produce significant error. Taking such issues into account, a form of Green's Theorem was applied to evaluate the two variable integrals in the LAVD formulation as parameterised line integrals. This avoids the difficulties found with interpolation on time-dependent domains and simplifies the double integral to a single integral.

Green's Theorem, for a vector field $\mathbf{v} = (u, v)$ can be stated

$$\oint_{\partial U(t)} u dx + v dy = \iint_{U(t)} \frac{\partial v}{\partial x} - \frac{\partial u}{\partial y} dA$$

for a time dependent domain $U(t)$ with boundary $\partial U(t)$ (Marsden and Tromba, 1985).

Green's Theorem may be used to evaluate both $vol(U(t))$ and $\int_{U(t)} \omega(\mathbf{x}, t) dV$ in calculating $\bar{\omega}$. To evaluate $vol(U(t))$ we choose $u = \frac{-y(p)}{2}$ and $v = \frac{x(p)}{2}$, so that the RHS of Green's becomes an area integral for the domain, where $x(p)$ and $y(p)$ are the boundary coordinates for $U(t)$, parameterised by p . To evaluate $\int_{U(t)} \omega(\mathbf{x}, t) dV$ we let u and v be the velocity field components and hence the RHS of Green's becomes the area integral of the third component of the vorticity, as required. MATLAB's `boundary()` function, which can extract the ordered set of boundary points for sufficiently convex domains, was used to extract the boundary point set for the initial rectangular grid. This set of points was then advected to the appropriate time t to be used in the numerical implementation of Green's formula to evaluate $\bar{\omega}$.

Lastly, the outermost and innermost closed convex contour curves of the LAVD field must be extracted. Despite the relative rigor of the LAVD formulation, numerically defining *outermost*, *innermost* and *convex* inserts a degree of subjectivity in the LCS extraction. In Haller's (2016) numerical implementation of LAVD, outermost (innermost) convex curves are identified as those surrounding a single turning point of the LAVD field with maximum (minimum) arclength above a certain threshold and *convexity deficiency* below a maximum value. Such definitions thus require two thresholds to be selected, d_{max} , the maximum convexity deficiency, and l_{min} , the minimum arclength, for the extraction of LCS from a LAVD field. Following Haller's approach, the convexity deficiency is calculated as the percentage difference between the area of the convex hull formed by the advected particle positions at a time t and the that of the polygon formed by the boundary points of the advected particles. This was done using MATLAB's convex hull tool box, which finds the area of the convex hull of a set of points, and MATLAB's `polyarea` function, which finds the area inside the boundary points of a set.



6 Double-gyre flow

The velocity field commonly known as the double gyre is a flow often used in testing flow analysis techniques as it has a number of useful properties and its behaviour is well established. Although this flow has limited physical analogy, it possesses a time-independent domain and easily reduces to the steady case by letting a parameter be zero. Consequently, the double-gyre is suitable for assessing the effectiveness of an LCS extraction technique in two dimensions. The flow is described by the following velocity field (Shadden et al., 2005):

$$\begin{aligned}\mathbf{v} &= (u, v) \\ u &= -\pi A \sin(\pi f(x, t)) \cos(\pi y) \\ v &= \pi A \cos(\pi f(x)) \sin(\pi y) \frac{\partial f}{\partial x}\end{aligned}$$

where

$$\begin{aligned}f(x, t) &= a(t)x^2 + b(t)x \\ a(t) &= \epsilon \sin(\omega t) \\ b(t) &= 1 - 2\epsilon \sin(\omega t)\end{aligned}$$

Thus, selecting $\epsilon = 0$ the flow becomes time-independent and may be analysed by conventional steady flow analysis. As discussed, for an autonomous flow letting (1) be zero and finding the points which satisfy this requirement gives the *fixed points* of the flow, which form the centre of structures like sources, sinks and saddle points. From such analysis, we expect two saddle fixed points at either end of a central partition dividing the two gyres (see Figure 4). The upper fixed point will be attractive along the upper boundary, such that all trajectories along the boundary are attracted towards that point. The lower fixed point will be attractive along the central partition, such that all trajectories along the partition will travel towards the lower fixed point. We also expect a centre fixed point in the middle of each gyre. In the steady case, this implies that fluid will not travel across the central barrier and fluid particles initially in one gyre will tend to remain in that gyre.

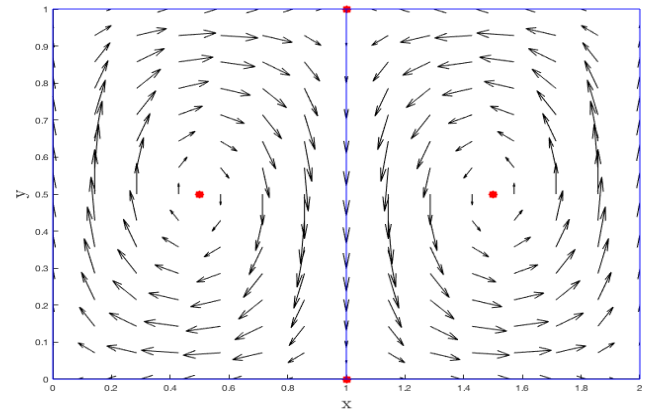


Figure 4: Phase space for Double Gyre flow, showing **fixed points** and **flow boundaries**.

Letting $\epsilon > 0$ we can produce Eulerian snapshots of the phase space at $t > 0$. The Eulerian picture shows the fixed points will oscillating from side to side as time is sequentially increased. From the Eulerian perspective, not



accounting for particle evolution trajectories, it would seem that the time-dependent double gyre periodically oscillates but is effectively autonomous if we were to consider a Poincare map of the flow. These observations of the Eulerian picture of the unsteady double gyre structure afford an interesting comparison to the following Lagrangian-based structural analysis, illustrating how structural information is lost if Lagrangian evolution is not taken into account in unsteady flow regimes.

6.1 FTLE field for Double-gyre flow

Setting $\epsilon = 0, 0.25, 0.75$, $A = 0.1$, $\omega = \frac{\pi}{5}$, the FTLE field was calculated for double-gyre flow in the time interval $[0, 15]$. This long time interval is necessary so that the FTLE field ridges become sufficiently narrow to outline ridges of maximal stretching when plotted.

Plots of the FTLE field calculated for $\epsilon = 0, 0.25, 0.75$ are shown in Figures 5, 6 and 7.

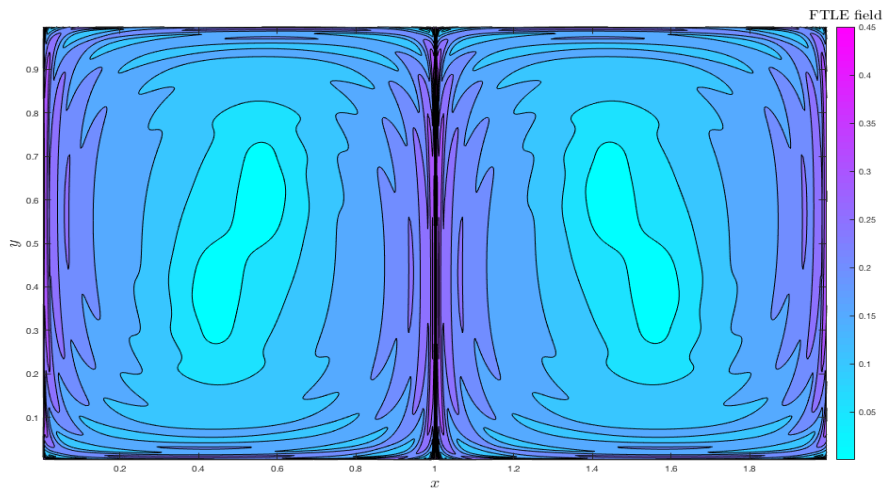


Figure 5: FTLE field for the double gyre when $\epsilon = 0$

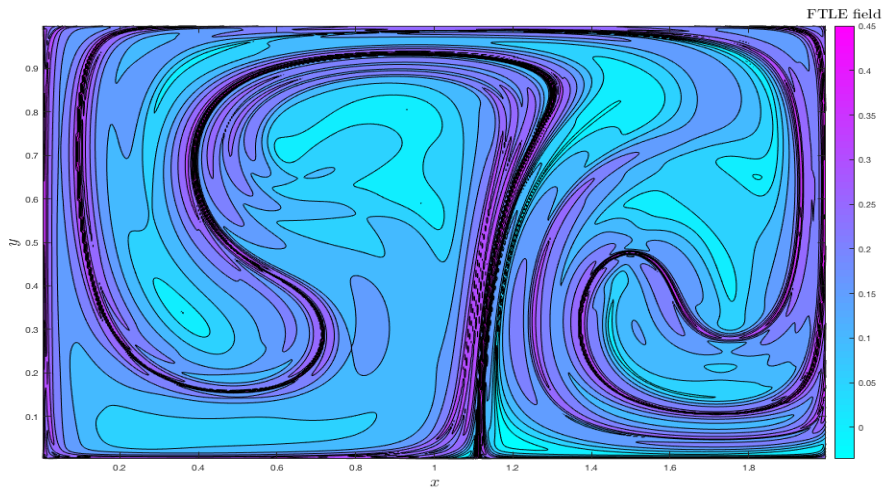


Figure 6: FTLE field for the double gyre when $\epsilon = 0.25$, $t = 15$

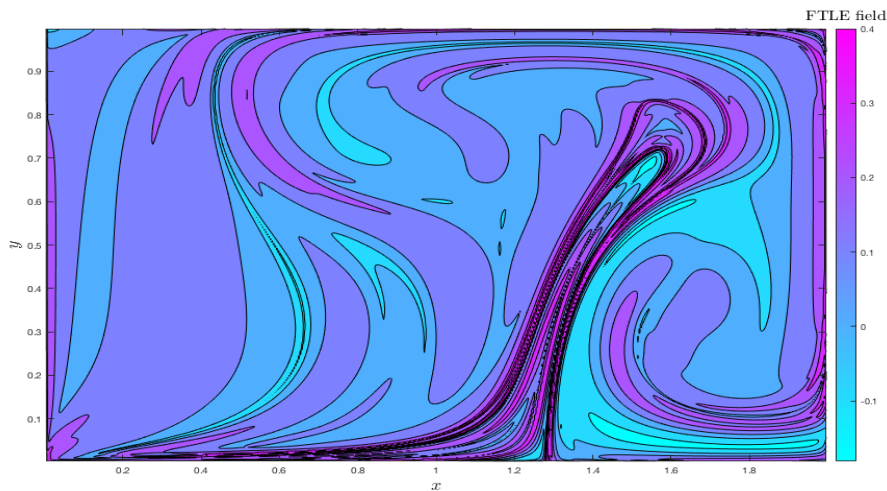


Figure 7: FTLE field for the double gyre when $\epsilon = 0.75$, $t = 15$

As can be seen from Figure 5, for $\epsilon = 0$, there is a strong FTLE ridge connecting the two saddle fixed points in the flow. This is intuitive, as it is expected that exponential stretching would occur most strongly along the trajectories of the phase space connecting the saddle fixed points, which are associated with stretching of fluid particles. The strongest FTLE ridge forms a barrier along which fluid particles flow from the upper fixed point, towards the lower fixed point and around one of the gyre boundaries, without entering either vortex. This picture agrees well with the phase space analysis for the steady case.

Comparing Figure 5 to Figure 6, it can be seen that with $\epsilon > 0$ the FTLE field can be considered as a perturbation of the autonomous case. The FTLE ridge present in the autonomous scenario becomes stretched and warped, curving inside and around each of the vortex centres. This can be attributed to the spatial oscillation of the fixed points which occurs over time for non-zero ϵ , causing fluid particles to now be drawn



towards two moving points in space. As this wobbling occurs, particles may be drawn close enough to the vortex centre that they rotate around it before being drawn back towards a moving fixed point. This highlights how the FTLE ridge technique may capture coherent structures arising from the induced time dependence of previously stationary structures.

This scenario is further exacerbated in Figure 7 for $\epsilon = 0.75$. The impermeability of the central barrier is broken down entirely in this case, with the greatest FTLE ridge stemming from the bottom fixed point and curling around the right most vortex centre. Run in backwards time, it is possible to capture similar behaviour in the leftmost vortex, with the central barrier oscillating between the two vortices over time. Thus, the FTLE ridge analysis highlights how particles beginning on the central partition are effectively stretched and folded continuously by travelling around the gyres when time dependence is induced. With a high degree of time dependence this leads to particles being drawn around and between the two vortices in a warped figure eight configuration.

6.2 LAVD field for Double-gyre flow

Setting $\epsilon = 0$ initially, the LAVD field was calculated for the double-gyre flow for increasing time intervals within $[0, 1]$, shown in Figure 8. In the steady case the LAVD field in this case is unchanged over time and agrees well with the phase space analysis. The regions surrounding the centre fixed points show as high LAVD field regions, which is expected as centre fixed points are associated with rotational motion.

Setting $\epsilon = 0.25, 0.75$, as shown in Figures 9-12, the oscillation of the ‘fixed’ points from side to side in the Eulerian viewpoint, translates to a loss of symmetry in the LAVD field. This loss of symmetry becomes increasingly notable as ϵ is increased. It can also be seen that increasing ϵ causes the two vortical structures to begin to exchange fluid; there is no longer a minimal LAVD field partition between the two regions of highest LAVD field. Viewing the evolution of the LAVD field over time for a particular ϵ it can be seen how regions of highest LAVD field are transported across the domain, for example; for $\epsilon = 0.75$ initially the right-most structure has maximum LAVD, while at $T = 1$ there are three structures present with maximal LAVD values. This suggests that the exchange of fluid which occurs for high ϵ induces the formation of additional vortical structures besides the two gyres.

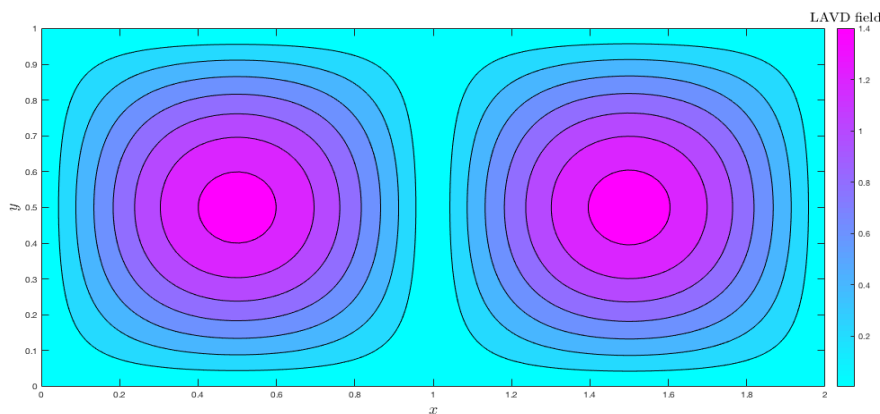


Figure 8: LAVD field for the double gyre when $\epsilon = 0$

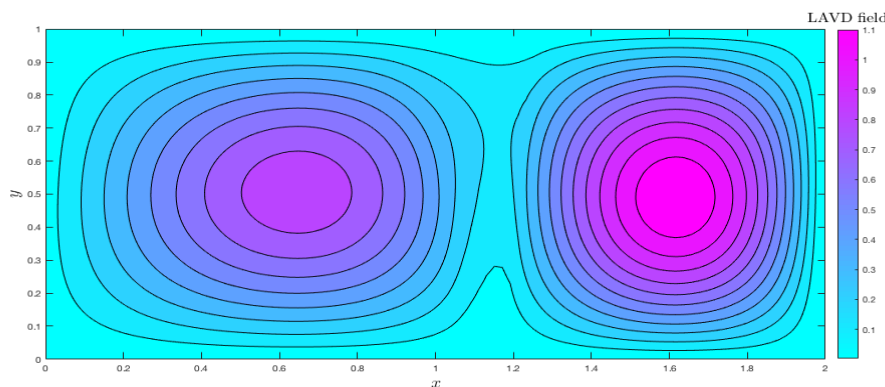


Figure 9: LAVD field for the double gyre when $t = 0.5, \epsilon = 0.25$

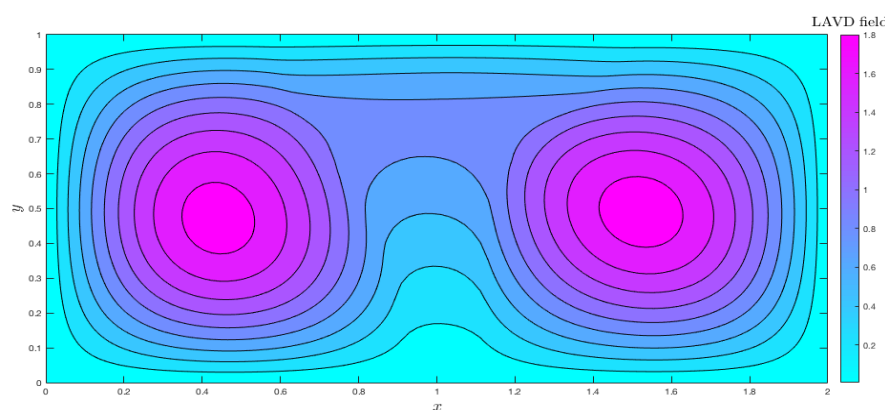


Figure 10: LAVD field for the double gyre when $T = 1, \epsilon = 0.25$

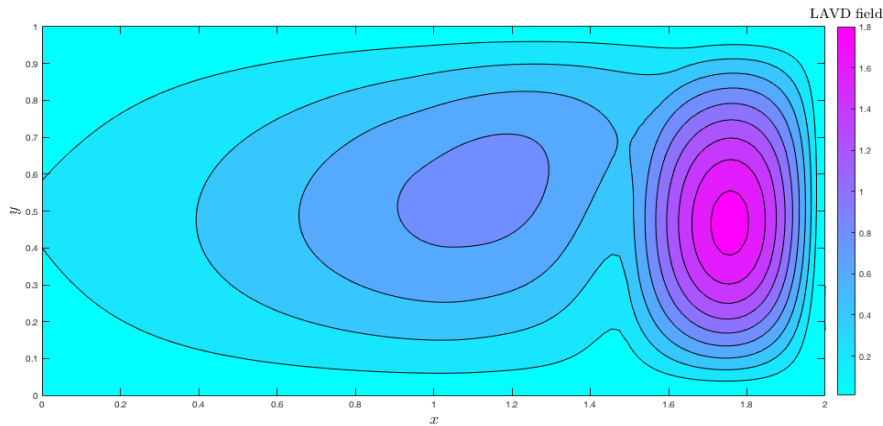


Figure 11: LAVD field for the double gyre when $T = 0.5, \epsilon = 0.75$

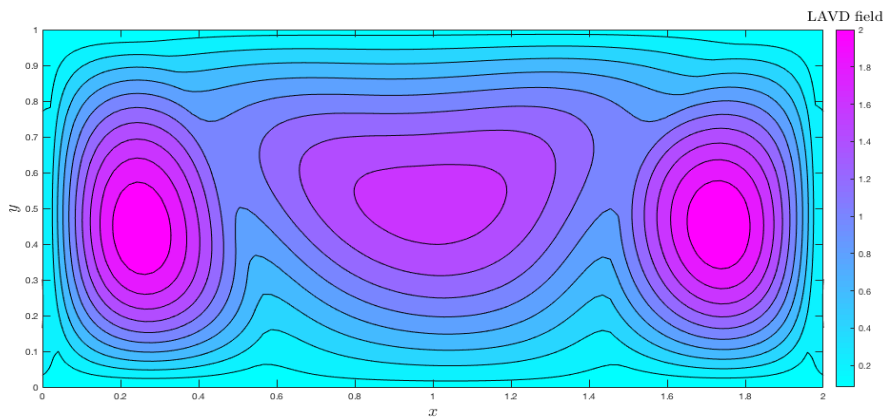


Figure 12: LAVD field for the double gyre when $T = 1, \epsilon = 0.75$

LAVD level curves satisfying Haller's convexity deficiency and arclength requirements were also extracted using a convexity deficiency threshold of $d_{max} = 10^{-3}$ and minimum arclength of $l_{min} = 0.3$. These thresholds were found by trial and error. In particularly filamented regimes, Haller's method would often pick up multiple smaller curves surrounding a larger rotational structure so parameters were adjusted until only larger, subjectively significant rotational structures were extracted. Figures 13-16 show the extracted LAVD curves for $\epsilon = 0.05, 0.25, 0.5, 0.75$.

From these figures, it can be seen that the extraction technique is reasonably effective in that the curves extracted coincide with the regions of highest LAVD field shown in Figures 8-12. Viewing the curves gives a less informative but clearer picture of the flow structure, showing the centres of the rotational structures present and their approximated outer boundaries. Plotting these curves at increasing times allows an appreciation of how the gyre structures grow and shrink in size over time and how their centres are translated across space. Comparing the $\epsilon = 0.05$ case to $\epsilon > 0.05$, it can be seen how the uniformity in size and position of the gyres



over time decreases as time dependence is increased.

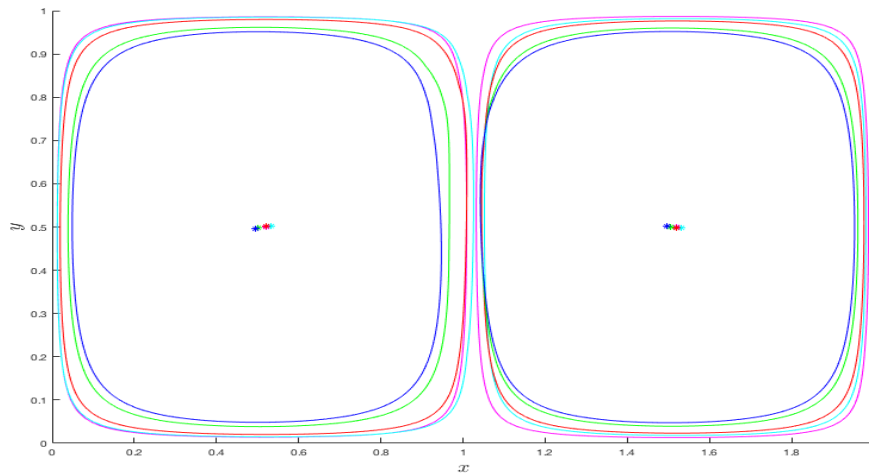


Figure 13: Outermost convex contours and their centres for the LAVD field when $T = 0$, $T = 0.2$, $T = 0.4$, $T = 0.6$, $T = 1$, $\epsilon = 0.05$

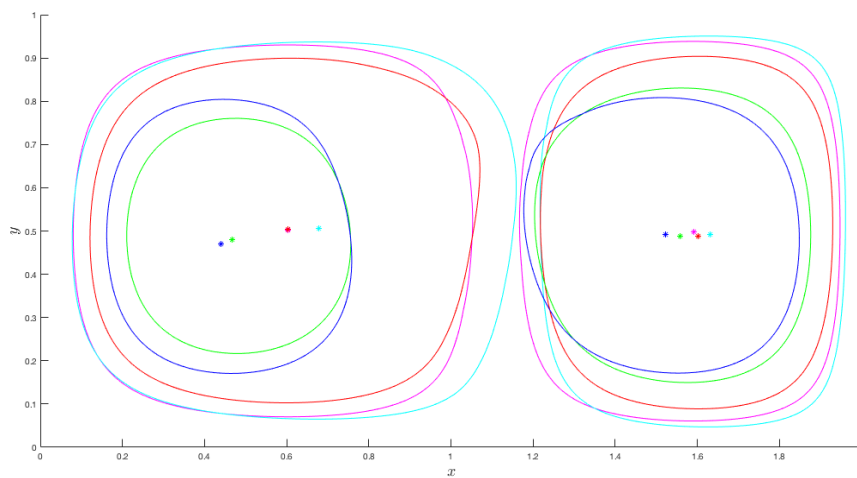


Figure 14: Outermost convex contours and their centres for the LAVD field when $T = 0$, $T = 0.2$, $T = 0.4$, $T = 0.6$, $T = 1$, $\epsilon = 0.25$

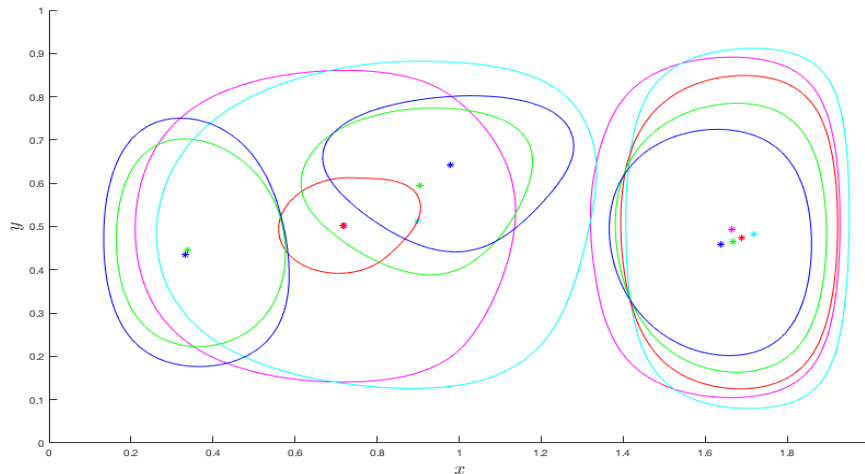


Figure 15: Outermost convex contours and their centres for the LAVD field when $T = 0$, $T = 0.2$, $T = 0.4$, $T = 0.6$, $T = 1$, $\epsilon = 0.5$

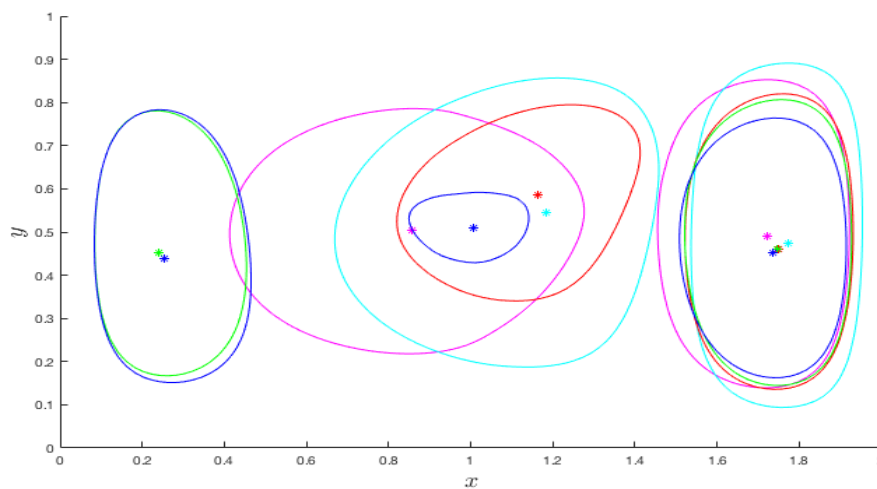


Figure 16: Outermost convex contours and their centres for the LAVD field when $T = 0$, $T = 0.2$, $T = 0.4$, $T = 0.6$, $T = 1$, $\epsilon = 0.75$

6.3 Findings from double gyre structural analysis

From the analysis of the double gyre's structure using these two methods, it can be seen that FTLE and LAVD both agree well with the phase space analysis in the steady case. The FTLE ridges pick up the exceptional stretching occurring along unidirectional lines of the flow velocity field connecting saddle fixed points, while the LAVD field picks up the rotational structures surrounding centre fixed points.

In the unsteady case, however, the analysis using these Lagrangian techniques affords considerable additional information compared to that given by simply viewing the phase space at a particular point in time. Viewing Eulerian snapshots of the phase space at consecutive times for the double gyre would suggest that



the two rotational gyre structures oscillate from side to side over time, carrying their associated ‘fixed’ points with them. However, from the FTLE ridges for the unsteady flow it can be seen how the dominant stretching structure evolves, being drawn from the bottom saddle-fixed point towards the top saddle fixed point. It is then thrown off its course by the time-dependent oscillation of the gyres and drawn towards the centre of the left-most gyre. The stretching structure then travels around the left-most gyre before being drawn back towards the upper saddle fixed point and into the right most gyre. This gives a vivid picture of how inducing time-dependence causes trajectories of exceptional stretching to be transported along a trail of moving points of attraction, breaking the impermeable barrier between the two gyres and producing a butterfly-like formation. The LAVD field in the unsteady case also shows how the two previously unconnected gyre structures begin to feed into each other as a result of time-dependence. These observations suggest an interesting continuum of structures, ranging from pure rotational to pure strain, extant in unsteady flows. This is unlike in steady flows where stationary fixed points allow a definite partitioning of the flow into rotational and stretching regions.

Viewing the LAVD curves for various ϵ and at increasing times, these curves provide a simplified picture of the rotational structures which is somewhat easier to analyse than the LAVD field, although information about the flow structure is lost. The curves and the field provide complementary information about the flow structure, although the trial and error nature of the curve extraction must be taken into account when analysing structures using both. Ideally some sort of parameter space analysis for l_{min} and d_{max} should be undertaken to reduce subjectivity in curve extraction, but this is a whole other domain of the research undertaken here which could be investigated.

Figures 17 and 18 show animations of the LAVD and FTLE fields for double gyre flow with $\epsilon = 0.25$ and $T \in [0, 15]$. Comparing these animations, it can be seen how these two techniques complement each other, showing how rotational and stretching structures evolve around each other in the flow. The animations also show how, on larger time frames, the flow’s rotational and stretching structures begin to wrap around each other and are broken into multiple smaller structures.

7 Rossby Wave flow

Having trialled the relatively simple double-gyre flow on the code written to compute the LAVD and FTLE fields, the numerical implementation was applied to the more complex, and more interesting, Rossby wave flow. This flow type is analogous to the atmospheric jets encircling Earth’s North pole, consisting of a fluid stream snaking around upper and lower vortex structures, as shown in Figure 19. The velocity field for this flow regime is

$$\mathbf{v} = (u, v)$$

$$u = -Al_1 \cos(l_1 y) \sin(k_1(x - c_1 t)) - \epsilon l_2 \sin(k_2(x - c_1 t)) \cos(l_2 y)$$

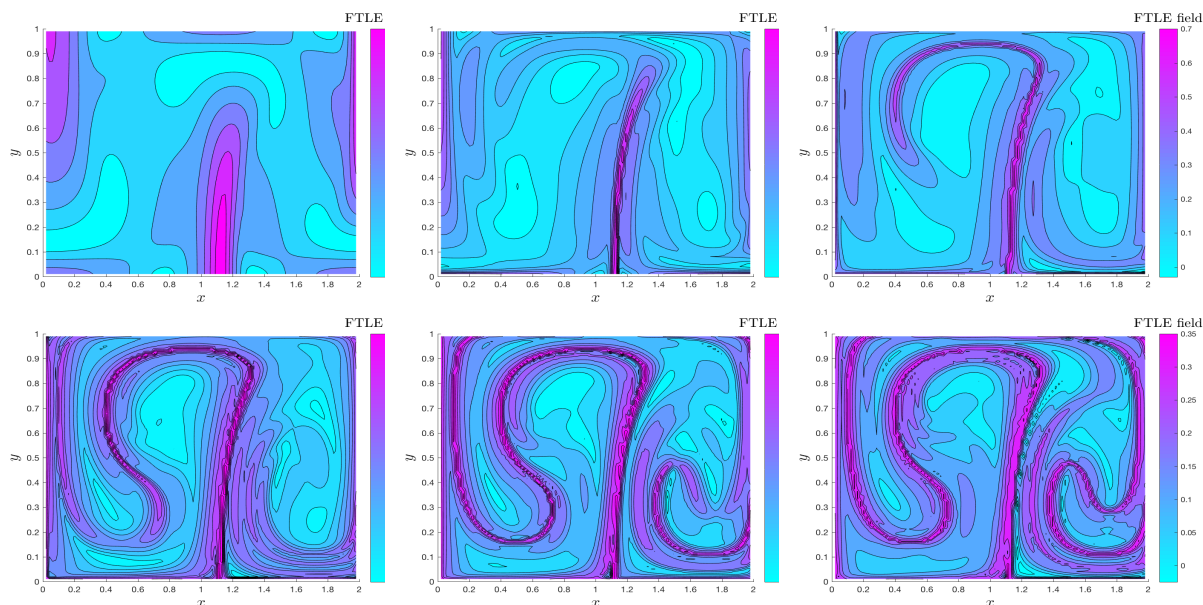


Figure 17: FTLE field for double gyre flow $T \in [0, 15]$, $\epsilon = 0.25$ for successively increasing time periods

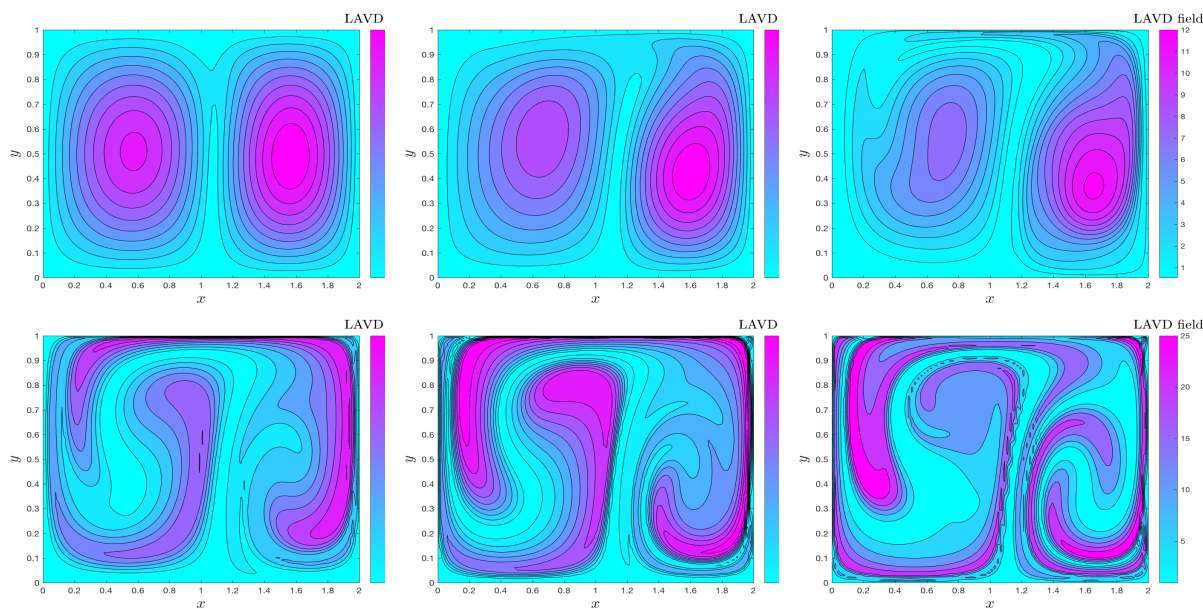


Figure 18: FTLE field for double gyre flow $T \in [0, 15]$, $\epsilon = 0.25$ for successively increasing time periods



$$v = Ak_1 \cos(k_1(x - c_1t)) \sin(l_1y) + \epsilon k_2 \cos(k_2(x - c_2t)) \sin(l_2y)$$

where $c_j = \frac{-1}{(k_j^2 + l_j^2)}$, $l_1 = 1$, $k_1 = 1$ and $k_2, l_2 \in \mathbb{Z}$.

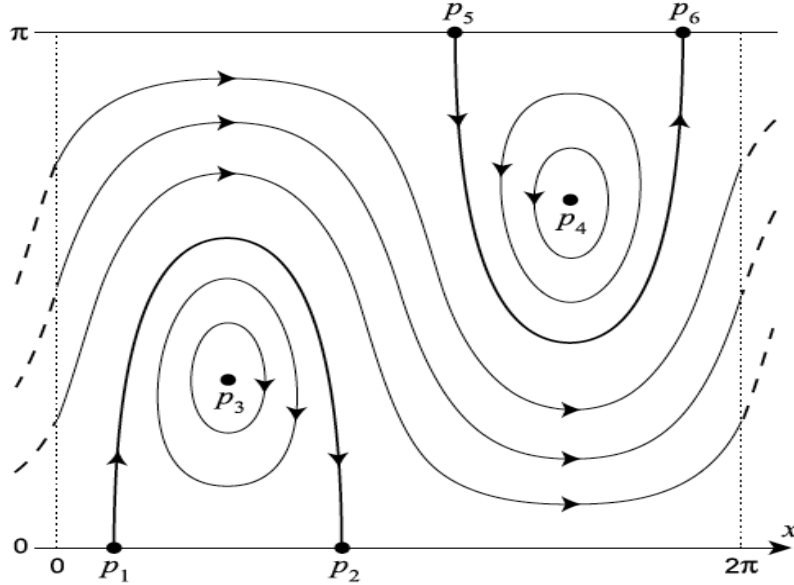


Figure 19: P_3, P_4 are centre fixed points, P_1, P_2, P_5, P_6 are saddle-like fixed points (Samelson and Wiggins, 2005).

Unlike double-gyre flow, this flow field possesses a time dependent domain and hence requires the use of Green's Theorem in the calculation of the LAVD field discussed previously. It is such flows with time dependent domains for which steady flow analysis methods may provide misleading information. Consequently, it is for these flows that the information afforded by LCS techniques such as LAVD and FTLE offers important insight.

7.1 FTLE field for Rossby Wave flow

Setting $A = 1, k_1 = 1, k_2 = -2, l_1 = 1, l_2 = 2, c_1 = -1/2, c_2 = -1/8$, the FTLE field was calculated for double-gyre flow in the time interval $[0, 15]$. As can be seen from Figures 20-23, the degree of exponential stretching increases with reasonable sensitivity to increases in ϵ . An increase from 0 to 0.25 shows how initially a single FTLE ridge separates the vortex and stream regions, while multiple stretching structures develop and begin to fold inside each other in the vortex regions as time dependence is increased.

In the steady case the particles initially in the vortices are confined to the vortex structures and will be generally restricted from entering the stream region due to the unbroken FTLE ridge encircling the two vortices.



As ϵ is increased, however the FTLE field ridges become increasingly broken and folded, allowing fluid to travel between the stream and vortex regions and hence between rotational and stretching structures. Interestingly, for very high ϵ , the stream and vortex regions become almost indiscernable, with FTLE ridges snaking between multiple smaller vortices scattered throughout the domain. This shows the high degree of filamentation and mixing for highly time-dependent rossby wave flow.

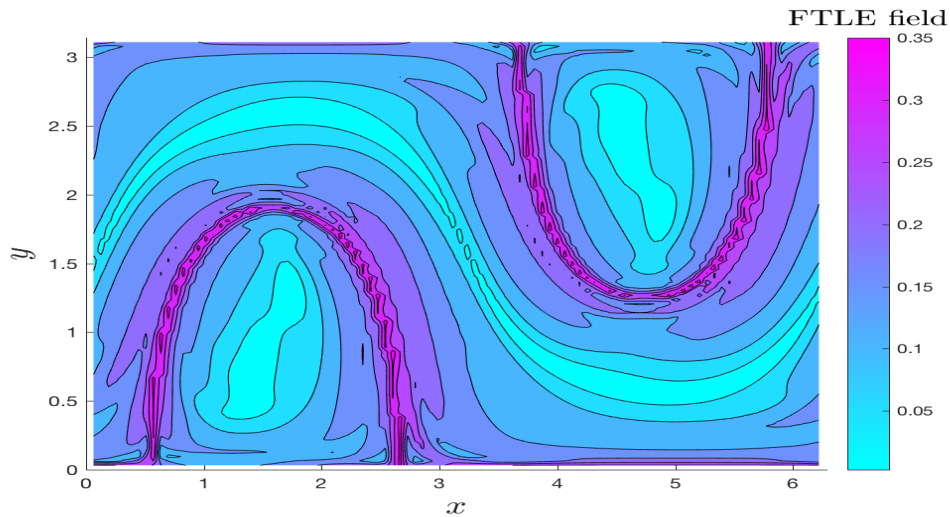


Figure 20: FTLE field for Rossby wave flow when $\epsilon = 0$

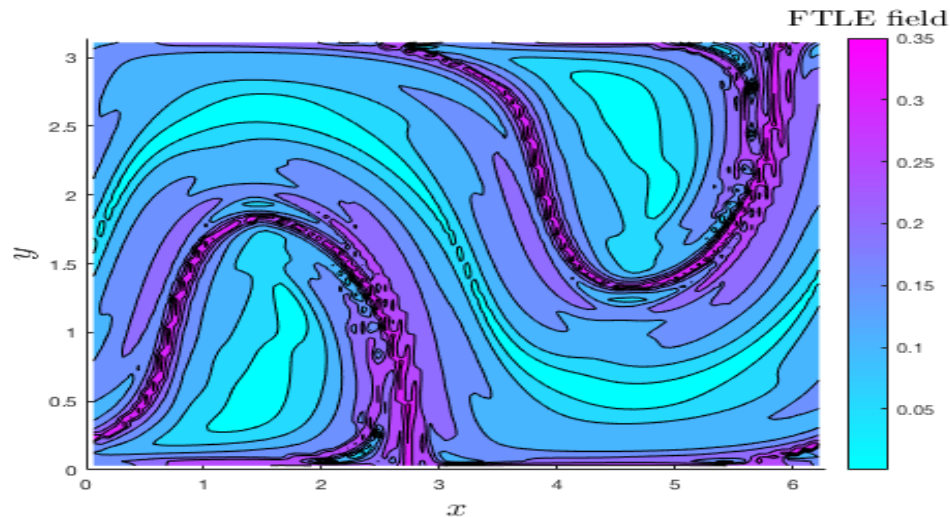


Figure 21: FTLE field for Rossby wave flow when $t = 15$, $\epsilon = 0.05$

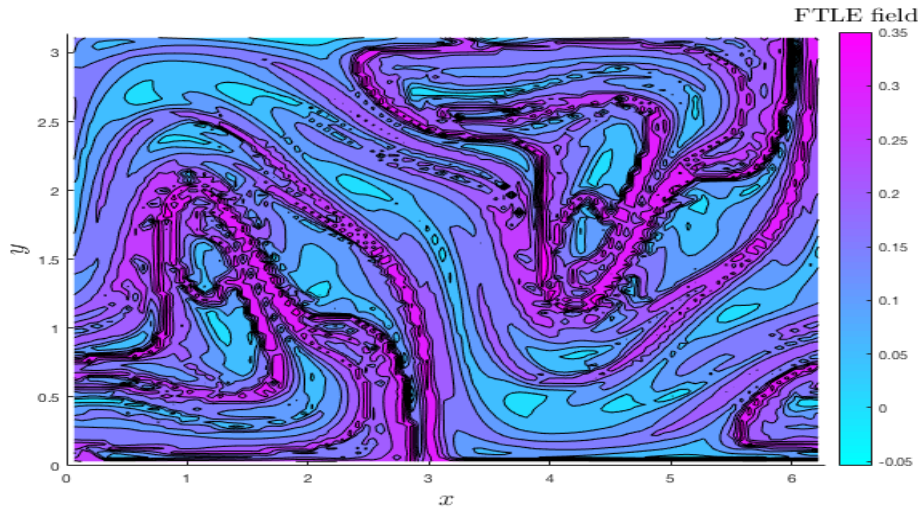


Figure 22: FTLE field for Rossby wave flow when $t = 15$, $\epsilon = 0.25$

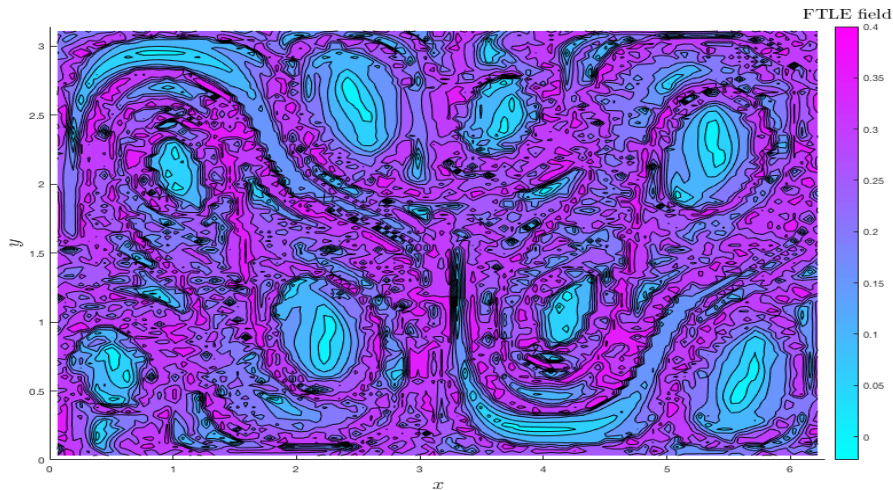


Figure 23: FTLE field for Rossby wave flow when $t = 15$, $\epsilon = 0.75$

7.2 LAVD field for Rossby Wave flow

As can be seen from Figure 24, the LAVD field for steady Rossby Wave flow highlights the upper and lower vortices as regions of maximal LAVD field. Interestingly, unlike the streamlines in Figure 19 would suggest, the structures illuminated are not entirely symmetric, showing how the rotational structures wrap anti-clockwise around the vortex centres, unlike in the double-gyre steady case where the rotational structures are circular and concentric. Additionally, high LAVD field structures appear to be present in the jet stream between the two vortices, probably due to the fluid particle trajectories in the stream wrapping around the vortices, producing a weaker rotational motion.

As ϵ is increased the upper and lower vortex structures appear to become increasingly unsymmetric, with their tips beginning to bend into the central stream region. The regions of high LAVD field also become increas-



ingly fragmented. For $\epsilon = 0.25$ this fragmentation is particularly significant around the vortex/stream boundary, indicating the increasing exchange between the stream and vortex regions of the flow.

For very high ϵ ($\epsilon = 0.50, 0.75$), the vortex and stream regions become indistinguishable from the LAVD field, giving way to multiple smaller vortex-like structures surrounded by intricately snaking streams, much like for the FTLE field. Interestingly, despite the complexity of the structures present in this case, there is a certain symmetry present in the high ϵ case in that the left and right regions of the field appear to be rotated versions of each other.

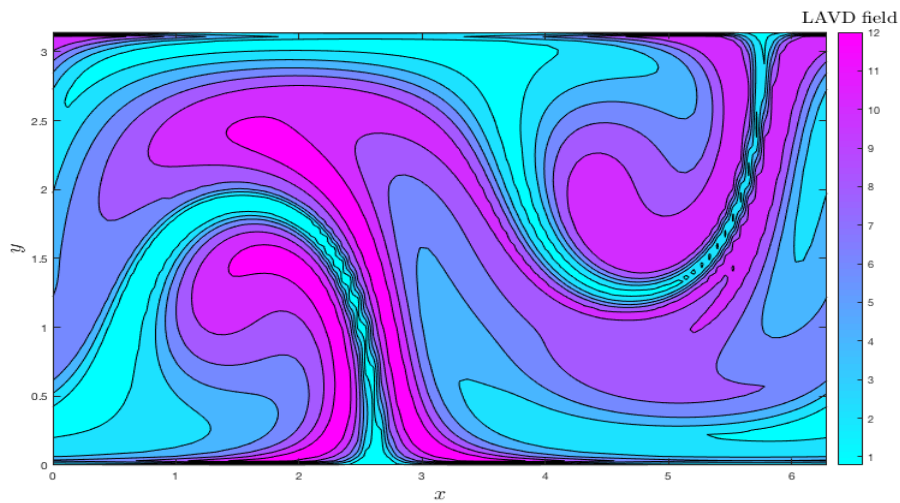


Figure 24: LAVD field for Rossby wave flow when $\epsilon = 0$

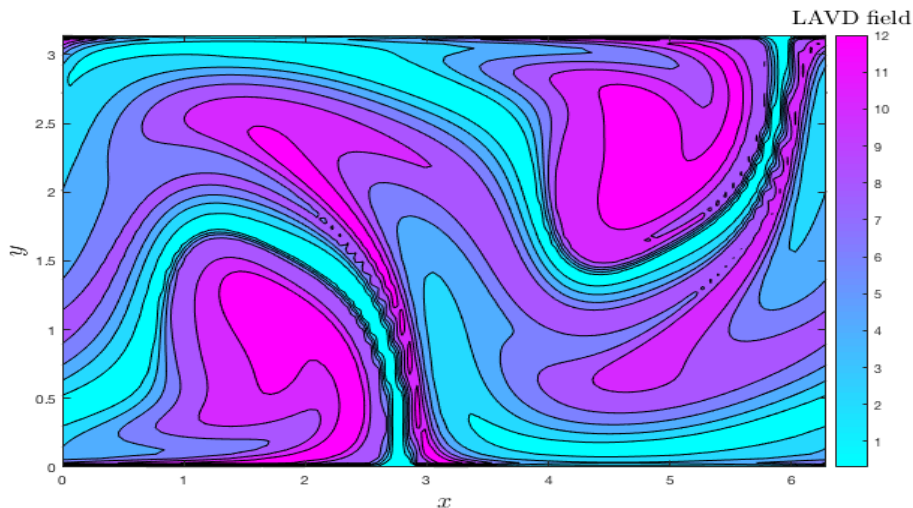


Figure 25: LAVD field for Rossby wave flow when $t = 1, \epsilon = 0.10$

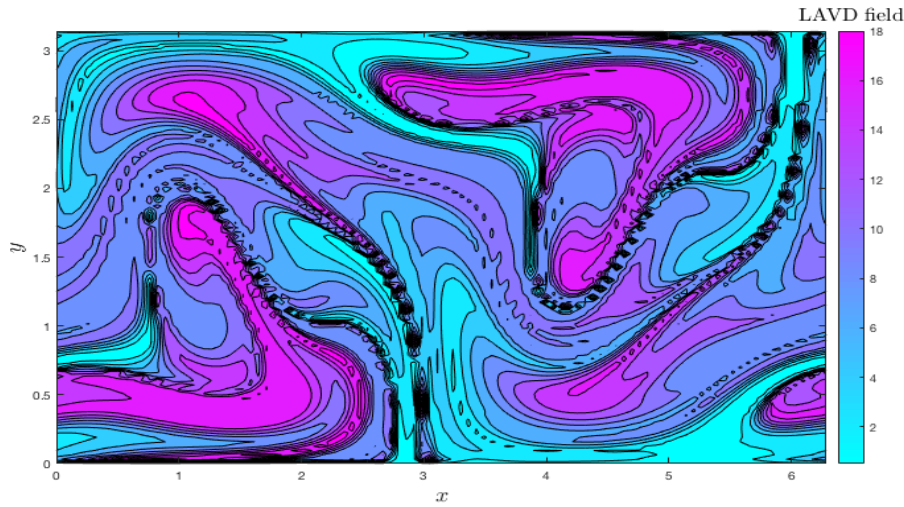


Figure 26: LAVD field for Rossby wave flow when $t = 1$, $\epsilon = 0.25$

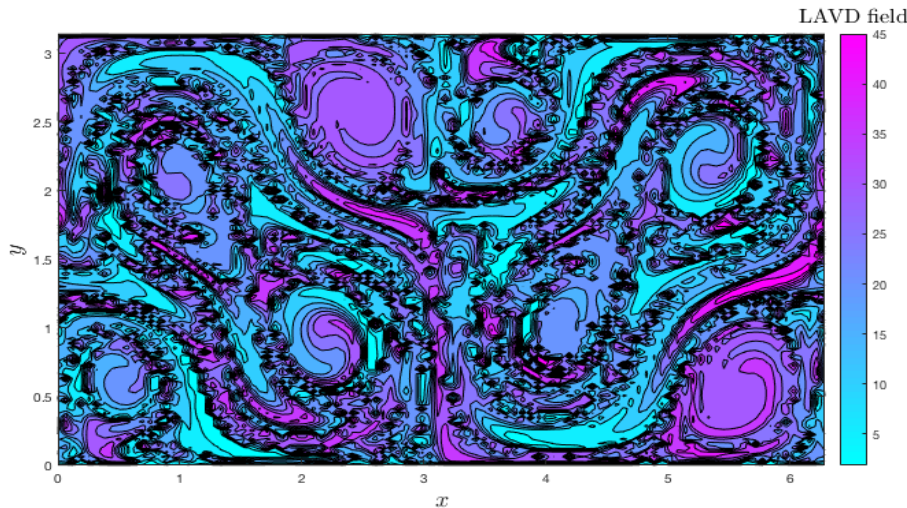


Figure 27: LAVD field for Rossby wave flow when $t = 1$, $\epsilon = 0.75$

It was attempted to find parameters for curve extraction for the LAVD field for rossby wave flow, however, suitable parameters were not found via trial and error within the time frame of the project. This is likely due to the high degree of filamentation which occurs in the rossby wave flow regime for even small ϵ and t . This again brings up the issue of constructing methods which provide some discernment in choosing curve extraction parameters. It seems that the high degree of filamentation in more complicated flows causes curve extraction to become difficult with unnesscessarily numerous smaller curves being extracted. This suggests that extraction parameters should be more directly related to the degree of filamentation and be dynamically altered as time increases and the degree of filamentation increases, much like with dynamically chosen step sizes in numerical ODE solvers.

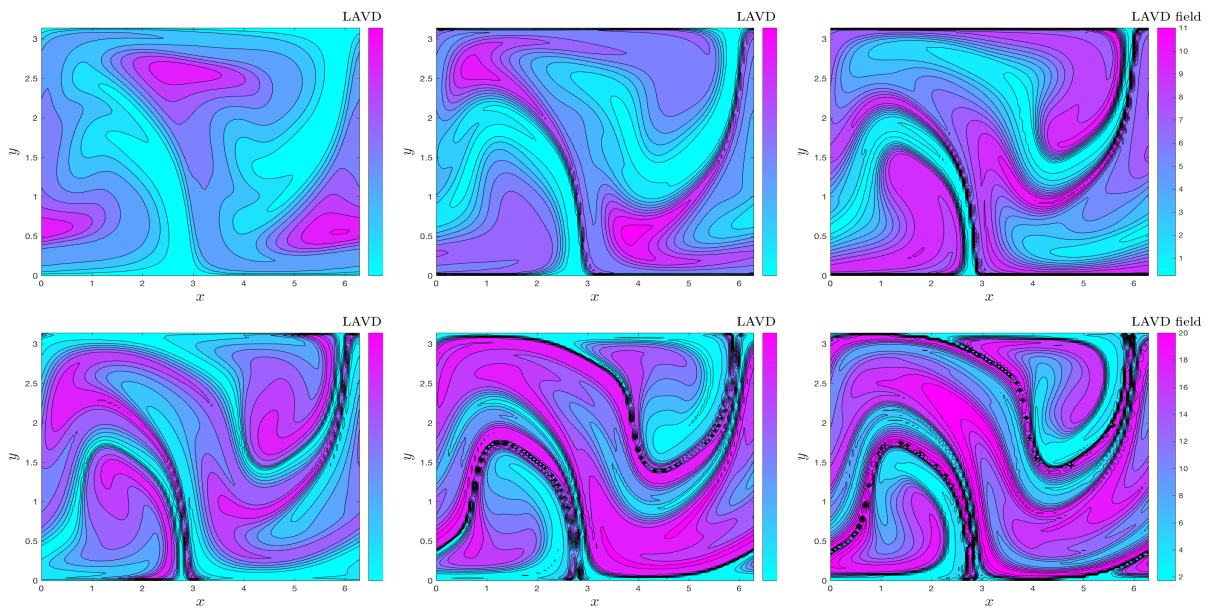


Figure 28: LAVD field for Rossby wave flow $T \in [0, 20]$, $\epsilon = 0.25$ for successively increasing time periods

7.3 Findings from Rossby Wave structural analysis

From the FTLE and LAVD fields for steady Rossby wave flow, it can again be appreciated how these techniques agree well with the phase space analysis in the steady case. The FTLE field picks up the stretching structure due to the stream curving around the two vortices, while the LAVD field picks up the rotational structures present around the centre fixed points at the middle of the two vortices.

In the unsteady case these techniques afford interesting structural information not available via phase space analysis, particularly due to the time dependent domain of Rossby Wave flow. The FTLE field elucidates how, as time-dependence is induced, the stream snaking between the two vortices begins to eat away at their rotational structure, pulling fluid from the vortices and into the stream. This again shows how fluid may travel between rotational and stretching structures for time-dependent flows. The LAVD field suggests that the interaction of the stream's stretching structure and the vortices' rotational structures causes the rotational structures to break up into smaller and smaller vortical structures with intricate streams snaking around them over time. This indicates a high degree of mixing in this flow regime due to time-dependence and the interaction between rotational and strain structures that it induces.

Figures 28 and 29 show animations of the Rossby wave LAVD and FTLE fields for $\epsilon = 0.25$ for increasing time intervals in $[0, 20]$. From these animations it can be appreciated how these techniques complement each other, but also give a comprehensive picture of the Lagrangian evolution of the flow structure.

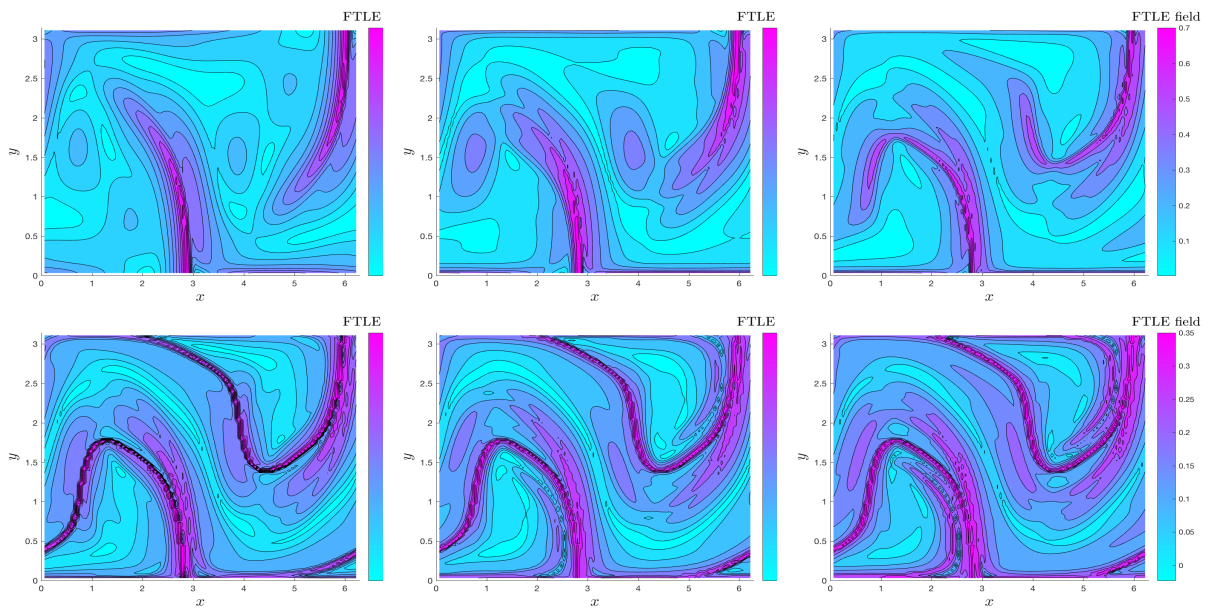


Figure 29: FTLE field for Rossby wave flow $T \in [0, 20]$, $\epsilon = 0.25$ for successively increasing time periods

8 Conclusions and Summary

Seeking techniques to extract coherent flow structures from unsteady flows we must consult theoretical frameworks of greater generality and complexity than in the case of steady flows. In unsteady flows the structures sought are time-dependent and, although we may draw steady flow structural analogies to guide us, what is meant by ‘coherent’ must be reassessed to encompass the wide variety of persistent structures observed in real-world flows. As discussed, a means of incorporating time dependence into a definition of coherent structures is by considering the Lagrangian flow map. A Lagrangian Coherent Structure can then be defined as an entity arising from the application of some criterion to the flow map via a procedure. In this investigation two numerical procedures capable of extracting LCS were implemented; the FTLE field and the LAVD field. These two procedures seek to isolate two different structural aspects of the flow: the stretching component and the rotational component respectively. Numerical schemes to calculate the FTLE and LAVD fields were trialed on two flow types possessing rotation- and stretching-dominated regions; double gyre and Rossby wave flow. From implementing FTLE and LAVD on these flows, some key findings can be appreciated:

- In the time independent case, both techniques agree well with the steady-case phase space analysis.
- Considering the distinctions between these two techniques gives insight into both the type of structure (rotational or stretching) and how these structures evolve and interact dynamically.
- The incorporation of time-dependence into these techniques also allows insight into how either stretching or rotation may dominate in particular regions over time and how predominantly rotational-type structures may temporally evolve into stretching-type structures. This suggests that, when time-dependence is induced, the structural categories which can be identified in the unsteady case, such as sinks, sources and



saddles, become less immutably defined as they interact with neighbouring structures.

- Although the theoretical background of these techniques is relatively rigorous in its derivation, numerical implementation may require the introduction of constructed thresholds which bare no direct relation to the theory. For example, the LAVD technique requires minimum arclength and maximum convexity deficiency parameters which were contrived using trial and error. This highlights how a certain subjectivity is present in numerically implementing this technique, despite a reasonably strong theoretical basis. Whether such subjectivity can be refined via some statistical mechanics techniques (for example selecting boundary curves possessing minimal entropy) would be an interesting area for further investigation.
- Time-dependent regions present interesting complications in the implementation of the LAVD technique; appealing to useful multivariable calculus theorems provides an effective means to address these complications. An interesting augmentation of the methods trialled in this project would be to apply Stoke's theorem in the numerical implementation of LAVD for flows possessing three spatial dimensions.

References

- S. Balasuriya. *Barriers and Transport in Unsteady Flows: A Melnikov Approach*. Series on Mathematical Modeling and Computation. Society of Industrial and Applied Mathematics Press, Philadelphia, 2016.
- S. Balasuriya, N.T. Ouellette, and I. Rypina. Generalized Lagrangian coherent structures. *Physica D*, 10.1016/j.physd.2018.01.011.
- G. Haller. Lagrangian coherent structures. *Annual Review of Fluid Mechics*, 47:137–62, 2015.
- G. Haller, A. Hadjighasem, M. Farazmand, and F. Huhn. Defining coherent vortices objectively from the vorticity. *Journal of Fluid Mechanics*, 795:136–173, 2016.
- R.A. Horn and C.R. Johnson. *Matrix Analysis*. Cambridge University Press, U.K., 1985.
- E.T. Kew, V. Rossi, J. Sudre, H. Weimerskitch, C. Lopez, E. Hernandez-Garcia, F. Marsac, and V. Garcon. Top marine predators track Lagrangian coherent structures. *Proceedings of the National Academy of Sciences*, 109(106):8245–8250, 2009.
- J.E. Marsden and A. Tromba. *Vector Calculus*. Cambridge University Press, U.K., 1985.
- I. Mezic, S. Loire, V.A. Fonoberov, and P. Hogan. A new mixing diagnostic and gulf oil spill movement. *Science*, 330:486–489, 2010.
- R.M. Samelson and S. Wiggins. Lagrangian transport in geophysical jets and waves. *Interdisciplinary Applied Mathematics*, 31:1–153, 2005.
- S.C. Shadden, F. Lekien, and J.E. Marsden. Definition and properties of Lagrangian coherent structures from finite-time Lyapunov exponents in two-dimensional aperiodic flows. *Physica D*, 212:271–304, 2005.